Atlantic Warm-Pool Variability in the IPCC AR4 CGCM Simulations

HAILONG LIU

Cooperative Institute for Marine and Atmospheric Studies, University of Miami, and NOAA/Atlantic Oceanographic and Meteorological Laboratory, Miami, Florida

CHUNZAI WANG

NOAA/Atlantic Oceanographic and Meteorological Laboratory, Miami, Florida

SANG-KI LEE AND DAVID ENFIELD

Cooperative Institute for Marine and Atmospheric Studies, University of Miami, and NOAA/Atlantic Oceanographic and Meteorological Laboratory, Miami, Florida

(Manuscript received 5 July 2011, in final form 27 March 2012)

ABSTRACT

This study investigates Atlantic warm pool (AWP) variability in the twentieth century and preindustrial simulations of coupled GCMs submitted to the Intergovernmental Panel on Climate Change (IPCC) Fourth Assessment Report (AR4). In the twentieth-century simulations, most coupled models show very weak AWP variability, represented by an AWP area index, because of the cold SST bias in the AWP. Among the IPCC models, a higher AWP SST index corresponds to increased net downward shortwave radiation and decreased low-level cloud fraction during the AWP peak season. This suggests that the cold SST bias in the AWP region is at least partly caused by an excessive amount of simulated low-level cloud, which blocks shortwave radiation from reaching the sea surface. AWP natural variability is examined in preindustrial simulations. Spectral analysis reveals that only multidecadal band variability of the AWP is significant in observations. All models successfully capture the multidecadal band, but they show that interannual and/or decadal variability is also significant. On the multidecadal time scale, the global SST difference pattern between large AWP years and small AWP years resembles the geographic pattern of the AMO for most coupled models. Observational analysis indicates that both positive ENSO phase and negative NAO phase in winter correspond to reduced trade winds in the AWP region. The westerly anomalies induced by positive ENSO and negative NAO lead to local heating and warm SST from March to May and February to April, respectively. This behavior as a known feature of anomalous AWP growth is well captured by only five models.

1. Introduction

The Western Hemisphere warm pool (WHWP), defined as the region with sea surface temperature (SST) warmer than 28.5°C, consists of the eastern North Pacific west of Central America, the ''IntraAmericas Sea'' (IAS) [i.e., the Gulf of Mexico (GoM) and the Caribbean Sea (CBN)], and the western tropical North Atlantic (TNA) (Wang and Enfield 2001, 2003). Unlike the Indo-Pacific warm pool, the WHWP is entirely north of the equator and is divided by the Central America landmass into two ocean regions: 1) the eastern North Pacific warm pool and 2) the Atlantic warm pool (AWP). Wang et al. (2006) show that the eastern North Pacific warm pool is more likely to follow El Niño–Southern Oscillation events since it is close to the ENSO region of maximum variance and is directly related to ENSO variability. AWP variability is, however, dominated by both local processes and remote forcing by climate patterns such as the Pacific ENSO (Covey and Hastenrath 1978; Nobre and Shukla 1996; Enfield and Mayer 1997; Lee et al. 2008; Enfield et al. 2006) and the North Atlantic Oscillation (NAO) (Grotzner et al. 1998; Giannini et al. 2001; Czaja et al. 2002, Enfield et al. 2006). The AWP shows strong variability on seasonal to multidecadal time scales (Wang and Enfield 2001, 2003; Wang et al. 2008b). For the

Corresponding author address: Hailong Liu, RSMAS/CIMAS, 4600 Rickenbacker Causeway, Miami, FL 33149.
E-mail: hailong.liu@noaa.gov

DOI: 10.1175/JCLI-D-11-00376.1

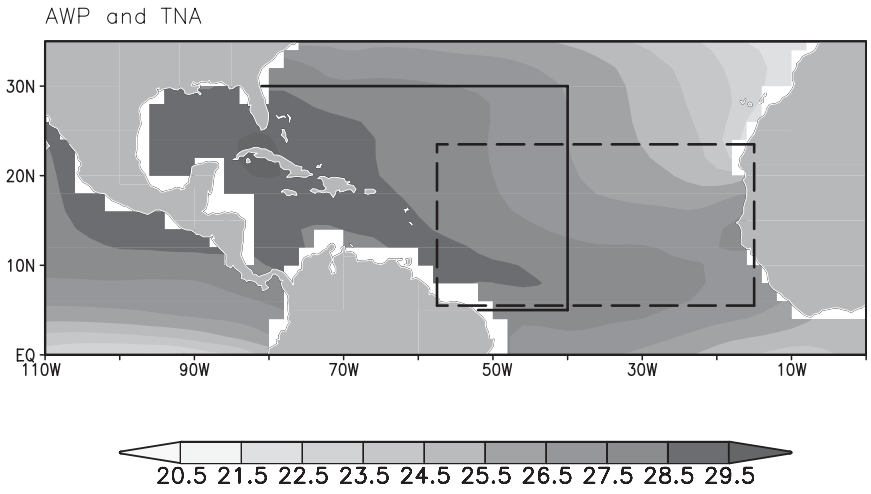

FIG. 1. Climatology of ERSST v3 in JASO. The dashed-line box shows the region of the tropical North Atlantic (TNA) (5.5°–23.5°N, 57.5°–15°W). The black box closed by land shows the region of AWP (5°–30°N, land–40°W) in which the AWP SST index (°C) (AWPTI) is defined.

annual cycle the AWP starts to develop in June while the earlier-developing warm pool in the eastern North Pacific (ENP) decays. During the four months July–October, the AWP reaches its maximum and decays quickly after October (Wang and Enfield 2003). Enfield and Lee (2005) showed that this seasonal variation is largely forced by the shortwave radiation, while the latent heat flux plays a secondary role particularly during the AWP decay phase. The roles of advection and turbulent mixing in the warm pool are also important for the AWP seasonal cycle. Lee et al. (2007) showed that the warm pool in the CBN region is affected by upwelling and horizontal advective cooling within and away from the coastal upwelling zone off northern South America during the onset and peak phases, thus slowing down the warm pool's development.

The AWP has substantial interannual fluctuations of area and intensity (Wang and Enfield 2003). Wang and Enfield found that the IAS lags Niño-3 by six months and is more highly and contemporaneously correlated with the TNA to the east. Years with a warm (cool) TNA tend to be years when the warm pool is larger (smaller) and the IAS is warm (cool). The correlations of the warm pool with the tropical Atlantic meridional gradient mode (AMM) (Servain 1991; Chang et al. 1997; Xie et al. 1999; Enfield et al. 1999; Xie and Carton 2004) and the Atlantic Niño (Zebiak 1993; Carton and Huang 1994; Latif and Grötzner 2000; Okumura and Xie 2006) are significant but relatively low, which suggest that the roles of AMM and the Atlantic Niño in the warm pool are smaller than those of the Pacific El Niño and TNA. This is consistent with the observation of Enfield et al. (1999) that the TNA and tropical South Atlantic are uncorrelated at zero lag and show different time scales of variability.

Much of the TNA variability is caused by remote forcing from climate variability outside the tropical Atlantic. Czaja et al. (2002) showed that almost all TNA SST extreme events can be related to either ENSO or NAO. Enfield et al. (2006) came to a similar conclusion to explain occurrences of large AWPs. Both ENSO and NAO lead to similar local response of the TNA: changes in surface winds induce changes of latent heat flux that in turn generate SST anomalies (e.g., Enfield and Mayer 1997). As the AWP is adjacent to the TNA and, in fact, includes the western TNA (Fig. 1), the remote forcings of ENSO and NAO act on the AWP in a similar way as on the TNA.

The Atlantic multidecadal oscillation (AMO) (Delworth and Mann 2000; Enfield et al. 2001; Bell and Chelliah 2006) is an oscillatory mode occurring in the North Atlantic SST primarily on multidecadal time scales. Wang et al. (2008a) showed that the AWP variability coincides with the signal of the AMO, that is, that the warm (cool) phases of the AMO correspond to larger (smaller) AWPs, and suggested that the multidecadal influence of the AMO on Atlantic tropical cyclone activity (Goldenberg et al. 2001) may operate through the mechanism of the AWP-induced atmospheric changes. Wang et al. (2011) showed that an eastward expansion of the AWP shifts the hurricane genesis location eastward. A large AWP also induces barotropic stationary wave patterns (Lee et al. 2009) that weaken the North Atlantic subtropical high and produce eastward steering flow anomalies along the eastern seaboard of the United States. Owing to these two mechanisms, hurricanes more frequently recurve toward the northeast without making landfall in the United States in the presence of an extremely large AWP.

Several studies have been conducted to evaluate the performance of coupled GCMs in the World Climate Research Program (WCRP) phase 3 of the Coupled Model Intercomparison Project (CMIP3) multimodel dataset (e.g., Lin et al. 2006; Saji et al. 2006; Miller et al. 2006; Joseph and Nigam 2006; Chang et al. 2007; Lin 2007; Richter and Xie 2008; de Szoeke and Xie 2008). Joseph and Nigam (2006), using six CGCMs, showed that, though the spatial SST pattern of ENSO is well captured, ENSO evolution is poorly represented and climate models are still unable to simulate many features of ENSO variability (Guilyardi et al. 2009) and its circulation and hydroclimate teleconnections to North America. Lin (2007) ascribed the cause of significant cold SST bias in much of the tropical ocean to the processes of strong trade winds, excessive latent heat flux, and insufficient shortwave flux. de Szoeke and Xie (2008) further concluded that both northeasterly winds across Central America in winter and meridional winds on the equator need to be improved in CGCMs for alleviating equatorial SST bias and improving simulation of ENSO and its teleconnections. The tropical Atlantic, compared with the other two major ocean basins, may be the most difficult to simulate in CGCMs. Chang et al. (2007) and Richter and Xie (2008) suggested that the warm SST bias of the Atlantic cold tongue region in CGCMs stems from the atmospheric component, which simulates too much rain over equatorial Africa and too little rain over the Amazon. This precipitation pattern weakens the Atlantic equatorial easterly winds, hampering development of the equatorial cold tongue.

In summary, AWP variability has been shown to affect precipitation patterns and tropical cyclone variability, based on observational analysis and AGCM simulations (Wang et al. 2006, 2008a,b). Therefore, it is necessary to evaluate how well current CGCMs represent AWP and its variability to improve coupled climate models for AWP research. In this study we analyzed 22 state-of-the-art CGCMs in WCRP CMIP3 multimodel dataset as to how they replicate observed AWP variability from seasonal to multidecadal time scales as well as the remote influences of ENSO and the NAO on the AWP.

The remainder of the paper is organized as follows. The models, validation datasets, and methods used in this study are described in section 2. AWP variability on different time scales in CGCMs is studied and compared with observational analysis in section 3. Section 4 summarizes the conclusions.

2. Data and methods

This study is based on a single run of the 22-CGCM output data from the climate of the twentieth century (20C3M) simulations and a single run of 16-CGCM output data from the preindustrial (PIcntrl) simulations in WCRP CIMP3 multimodel dataset, which are submitted to the Intergovernmental Panel on Climate Change (IPCC) Fourth Assessment Report (AR4). The modeling center and country, IPCC model ID, designated letter, abbreviation, and length of PIcntrl simulations for each model in this study are shown in Table 1. The model data can be downloaded from the website of Program for Climate Model Diagnosis and Intercomparison (PCMDI) (http://www-pcmdi.llnl.gov/). The 20C3M simulations are spun up and then forced by solar, volcanic, sulfate aerosol, and greenhouse gas forcings from different starting years (1850, 1860, 1870, 1890, or 1900) to 1999. Of the 22 models (Table 1, column 4), 3 models [CGCMt47 and CGCMt63 from the Canadian Centre for Climate Modeling and Analysis, and the MRI (Japan)] performed both heat and water flux corrections. One model, the INMCM (Russia), performed only a freshwater flux adjustment. All other CGCMs are coupled freely without flux correction. The PIcntrl simulations are used for the reference to the 20C3M experiments and also provide initial states for the 20C3M simulations. The initial state of PIcntrl is taken from the final state of a long term preindustrial spinup, which is a fully coupled time integration and is long enough to minimize potential climatic drift. The anthropogenic and natural forcing is fixed in PIcntrl simulationsand thus provides a direct data source to estimate the natural variability embedded in CGCMs. Variables of surface heat flux, wind stress, sea level pressure (SLP), and SST are used.

In this study, the 20C3M simulations are studied for the AWP climatology of CGCMs and compared with available observations. We focus on the natural variability of CGCMs (including AWP spectrum, interannual and multidecadal variability, and remote connection) of the PIcntrl simulations because of their long time series and embedded natural variability without being contaminated by the external forcing. Statistical analyses are used and wavelet software was provided by C. Torrence and G. Compo (Torrence and Compo 1998).

Observational datasets are used to validate the variabilities of CGCM simulations. SST data are the NOAA Extended Reconstruction Sea Surface Temperature version 3 (ERSST v3) (Smith et al. 2008). The temporal coverage is from January 1854 to the present. These data can be obtained online (http://www.ncdc.noaa.gov/oa/climate/research/sst/ersstv3.php). Surface fluxes and SLP data are from NOAA/Cooperative Institute for Research in Environmental Sciences (CIRES) Twentieth Century Global Reanalysis (20CR) version II (Compo et al. 2011). This atmospheric reanalysis spans the entire twentieth century (1871–2008), assimilating only surface observations of synoptic pressure, monthly SST, and sea ice distribution.

TABLE 1. Sixteen of the 22 models involved in this study and their IPCC ID, Letter denotation, short names used throughout the paper, and length in years of PIcntl simulations. Letter denotation is used in some figures in paper. Letter A stands for observations; see Fig. 10.

Sponsor, Country	IPCC ID, Vintage	Letter denotation	Abbreviation	Preindustrial control length used (yr)
Bjerknes Centre for Climate Research, Norway	BCCR-BCM2.0, 2005	B	BCM	NA
Canadian Centre for Climate Modeling and Analysis, Canada	CGCM3.1(T47), 2005	C	CGCMt47	300
Canadian Centre for Climate Modeling and Analysis, Canada	CGCM3.1(T63), 2005	D	CGCMt63	300
Météo-France/Centre National de Recherches Météorologiques, France	CNRM-CM3, 2004	E	CNRM	300
Commonwealth Scientific and Industrial Research Organization (CSIRO) Atmospheric Research, Australia	CSIRO-MK3.0, 2001	F	CSIRO30	300
	CSIRO-MK3.5	G	CSIRO35	NA
NOAA/Geophysical Fluid Dynamics Laboratory (GFDL), USA	GFDL CM2.0, 2005	H	GFDL20	300
	GFDL CM2.1, 2005	I	GFDL21	300
National Aeronautics and Space Administration/ Goddard Institute for Space Studies (GISS), United States	GISS-AOM, 2004	J	GISSaom	NA
	GISS-ER, 2004	K	GISSer	300
National Key Laboratory of Numerical Modeling for Atmospheric Sciences and Geophysical Fluid Dynamics/Institute of Atmospheric Physics, China	Flexible Global Ocean–Atmosphere–Land System Model gridpoint version 1.0 (FGOALS-g1.0), 2004	L	IAP	300
National Institute of Geophysics and Volcanology, Italy	INGV-ECHAM4	M	INGV	NA
Institute for Numerical Mathematics, Russia	INM-CM3.0, 2004	N	INMCM	300
Institut Pierre Simon Laplace, France	IPSL CM4, 2005	O	IPSL	300
Center for Climate System Research (University of Tokyo), National Institute for Environmental Studies, and Frontier Research Center for Global Change (JAMSTEC), Japan	MIROC3.2(hires), 2004	P	Mhires	100
	MIROC3.2(medres), 2004	Q	Mmedres	300
Max Planck Institute for Meteorology	ECHAM5/MPI-OM, 2005	R	MPI	NA
Meteorological Research Institute, Japan	MRI CGCM2.3.2, 2003	S	MRI	300
National Center for Atmospheric Research (NCAR), USA	CCSM3, 2005	T	CCSM3	300
	PCM, 1998	U	Npcm1	NA
Hadley Centre for Climate Prediction and Research/Met Office, United Kingdom	UKMO HadCM3, 1997	V	Uhadcm3	300
	UKMO HadGEM1, 2004	W	Uhadgem1	240

More information about this dataset is provided online (http://www.esrl.noaa.gov/psd/data/20thC_Rean/).

The AWP area index (AWPAI) is defined as the area inside the 28.5°C isotherm at the sea surface in the AWP region. The AWP SST index (AWPTI) is defined as the box-averaged SST from the American coast to 40°W and from 5° to 30°N. The AMO index is defined as the detrended area-weighted average over the North Atlantic from 0° to 70°N (Enfield et al. 2001). The Niño-3 index is an average of the SST anomalies in the region 5°N–5°S, 150°–90°W. The NAO index is chosen as the difference of normalized SLP between 39°N, 9°W (Lisbon, Portugal) and 65°N, 22°W (Stykkisholmur/Reykjavik, Iceland) (Hurrell 1995). All indexes are calculated for each model and observations.

A Taylor diagram (Taylor 2001) is applied to quantify how well models simulate an observed climate field. It relies on three nondimensional statistics: 1) the ratio of the variances of the two fields (r, which is the standard deviation of the model divided by standard deviation of the observations); 2) the correlation between the two fields (R, which is computed after removing the overall means); and 3) the rms error between models and observation (E, which is normalized by the standard deviation

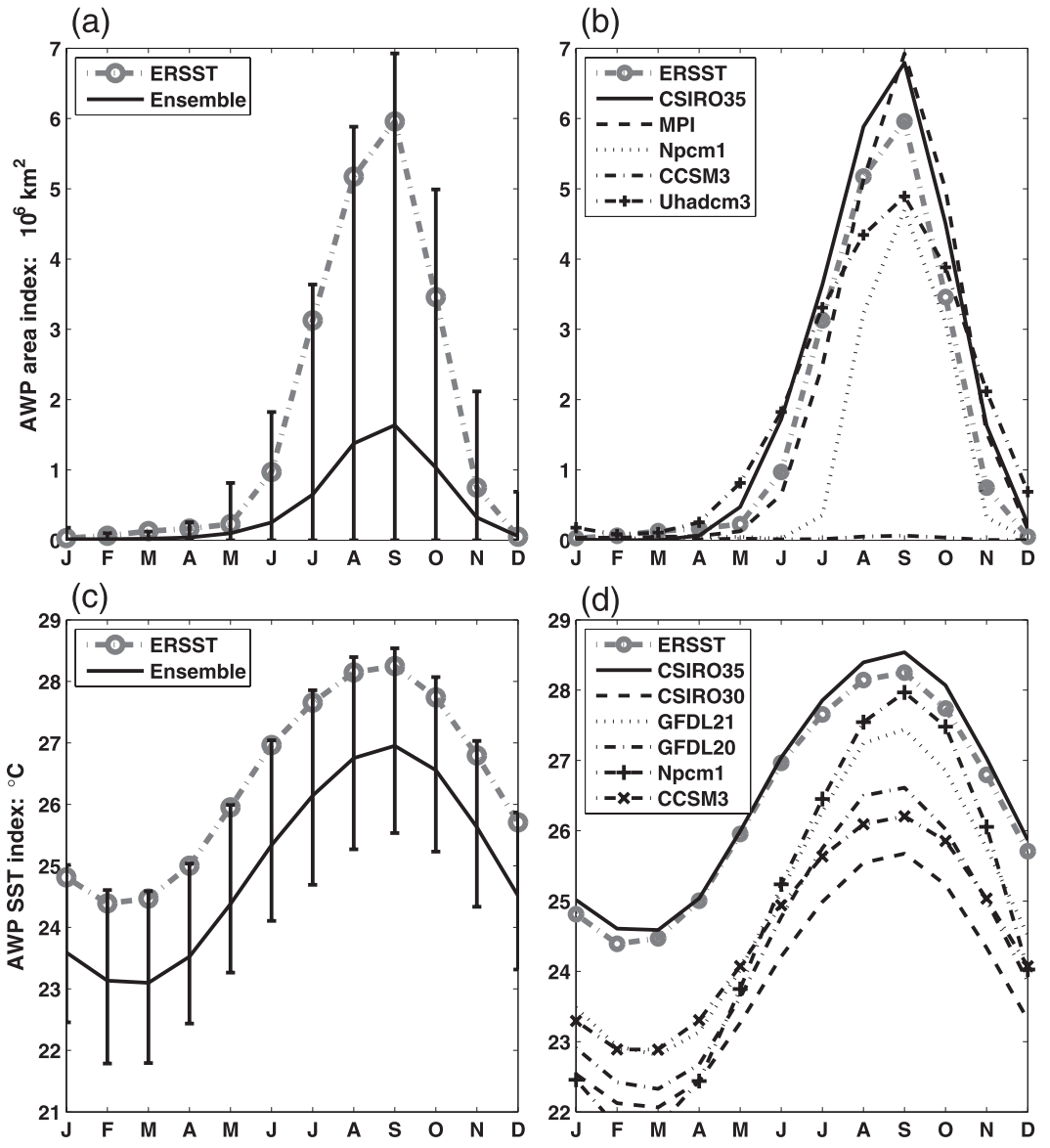

FIG. 2. (a) Seasonal cycle of the AWP area index (AWPAI). ERSST is shown in dash gray line. Ensemble of 22 models with spread bar is shown in black line; unit is 10^6 km^2. (b) Seasonal cycle of the AWPAI of selected models. (c) Seasonal cycle of the AWPTI. ERSST is shown in dash gray line. Ensemble of 22 models with spread bar is shown in black line. Unit is °C. (d) Seasonal cycle of the AWPTI for selected models. Model data are from 20C3M simulations.

of the observed field). This diagram provides a 2D graph based on the three statistics summarizing how closely a pattern matches observations.

3. AWP variability

a. Seasonal cycle

The AWPAI is shown in Fig. 2a and Fig. 2b. The AWP reaches its maximum during July–October and decays quickly after October (Wang and Enfield 2003). This seasonal cycle character is clearly seen in ERSST. The index of 22 models ensemble only has less than one-third of the ERSST index amplitude during the summer peak, even though the model spread covers from almost zero to four times the ensemble mean. Compared with ERSST, only four models have comparable amplitude (see Table 1, column 4): CSIRO35, MPI, Npcm1, and Uhadcm3 (in Fig. 2b). Seven models are able to simulate the seasonal cycle, but the amplitude is much weaker compared with ERSST: GFDL21, INGV, INMCM, Mhires, MRI, and Uhadgem1. For 11 models, the amplitude is too weak.

Three models, namely CCSM3 (shown in Fig. 2b as an example), BCM, and CNRM cannot capture a reasonable seasonal cycle. The weak seasonal cycles for the AWP area in most CGCMs are due to a cold SST bias in the AWP and TNA regions (Chang et al. 2007; Breugem et al. 2008; Richter and Xie 2008; Richter et al. 2011). This can be clearly seen in Fig. 2, wherein the seasonal cycle of AWPTI in the ensemble and most models is of comparable amplitude to observations (Fig. 2c), but the simulated area is much less (Fig. 2a).

The AWPAI is not suitable for interannual and multidecadal variability in this study as in some years this index cannot be computed for a part of the CGCMs due to the cold SST bias (Misra et al. 2009). Therefore, the AWPTI is used for this study. For the AWPTI (Figs. 2c,d), all 22 models used in this study capture the overall timing of the seasonal cycle which peaks in July–October, although some models lag the observation by about one month. The ERSST index and 22 model ensemble-mean index with spread are shown in Fig. 2c. The model spread is consistent throughout the year within a range of 2°–3°C. Four models well reproduce the observed seasonal cycle: CSIRO35, INGV, MPI, and Uhadcm3 (Fig. 2d). Although Npcm1 has a realistic AWPAI cycle, it has realistic SST performance only in the summer simulation, while in winter the cold SST bias reaches 3°C. As shown in Fig. 2d, CSIRO35 is much improved from CSIRO30. This improvement may be associated with the change to the surface drag formulation that accounts for the velocity of the ocean currents relative to the atmospheric surface velocity, and with the inclusion of an oceanic horizontal mixing parameterization due to wind-driven horizontal mixing by the passage of large- and small-scale atmospheric eddies (Gordon et al. 2010). GFDL21 is improved especially during summer compared with GFDL20. The possible causes are the improved simulations of surface wind stress in CM2.1 and changes in cloud tuning that act to increase the net surface shortwave radiation in CM2.1, thereby reducing the cold bias presented in CM2.0 (Delworth et al. 2006). This is supported by Fig. 3. The other models are also able to simulate the seasonal cycle but with lower SST (within 2°C less than ERSST) owing to the cold SST bias in the AWP region.

Wang and Enfield (2001) suggested that the SST seasonal variations in the AWP region are induced primarily by surface net heat flux with a phase lag of 3–4 months. The net surface heat flux consists of shortwave, longwave, latent, and sensible heat fluxes. The shortwave and latent heat fluxes are the two largest terms. The shortwave flux has maximum value from April to August, and the latent and sensible heat losses (heat loss means that ocean loses heat, heat gain means that ocean gains heat) have their minima around May. This results in the maximum of net heat flux occurring in late spring and maximum SST in fall. The relationship between heat fluxes and AWP SST is well reflected in 20CR (Figs. 3a–d) and also reflected in most of the 22 models. As already noted, the AWPTI of CSIRO35 is much improved compared with CSIRO30. From Fig. 3, the possible direct cause of this improvement is due to the increase of net surface heat flux. But, it does not hold true among the IPCC models that the higher net heat flux corresponds to higher AWPTI. Compared with 20CR, IPCC models have less latent heat loss, less shortwave heat gain, and more sensible heat loss. The latent heat flux bias of the models should warm the AWP, thus it is not the cause of the cold AWP bias in CGCMs. Shortwave radiation is too weak in CGCMs. The associated cooling compensates the warming due to latent heat flux bias. Among the IPCC models, higher AWP SST corresponds to more shortwave radiation (Fig. 4a) and less low-level cloud fraction (Fig. 4b) during the AWP peak season. It suggests that the negative SST bias in the AWP region is connected with an excessive amount of simulated low-level cloud, which blocks shortwave radiation from reaching the sea surface. This positive feedback of colder SST, increased fraction of low level cloud, and decreased surface shortwave flux may enhance the cold SST bias. However, it is not clear whether the excessive simulated clouds in CGCMs caused or are caused by the SST bias, as it is difficult to determine if the poor low-level cloud simulations in the CGCMs result from incorrect cloud or boundary layer parameterizations or from fundamentally different SST and wind distributions (Mansbach and Norris 2007).

The spatial pattern of seasonal SST bias in the tropical Atlantic is shown in Fig. 5. Figure 5a(1)–(4) show the SST spatial pattern based on ERSST in four seasons. The AWP exists in summer and fall. To compare with ERSST, the SST bias pattern is shown for the 22 member ensemble mean [Fig. 5b(1)–(4)] and for selected models: Figs. 5c(1) and 5e(4). The common character as shown in Fig. 3b(1)–(4) is that southeast Atlantic warm SST bias including the cold tongue and the Angola–Benguela coastal regions exists in each model for all four seasons. For the three models: CSIRO35 [Fig. 5c(1)–(4)], MPI, and Uhadcm3, there is also a warm bias in the North Atlantic region for all the seasons. For the other 19 models such as CCSM3 [Fig. 5d(1)–(4)], there is always a cold SST bias in the AWP region for all seasons even though the cold bias, such as in INGV [Fig. 5e(1)–(4)] is very small. It is possible that the opposite biases north and south of the equator are linked through tropical Atlantic variability (TAV) (Xie and Carton 2004). The warm bias in the southeast tropical Atlantic may cause the cold bias north of the equator via the feedback of wind, evaporation, and SST. The seasonal consistency of the SST bias and the biased spatial pattern need further analysis.

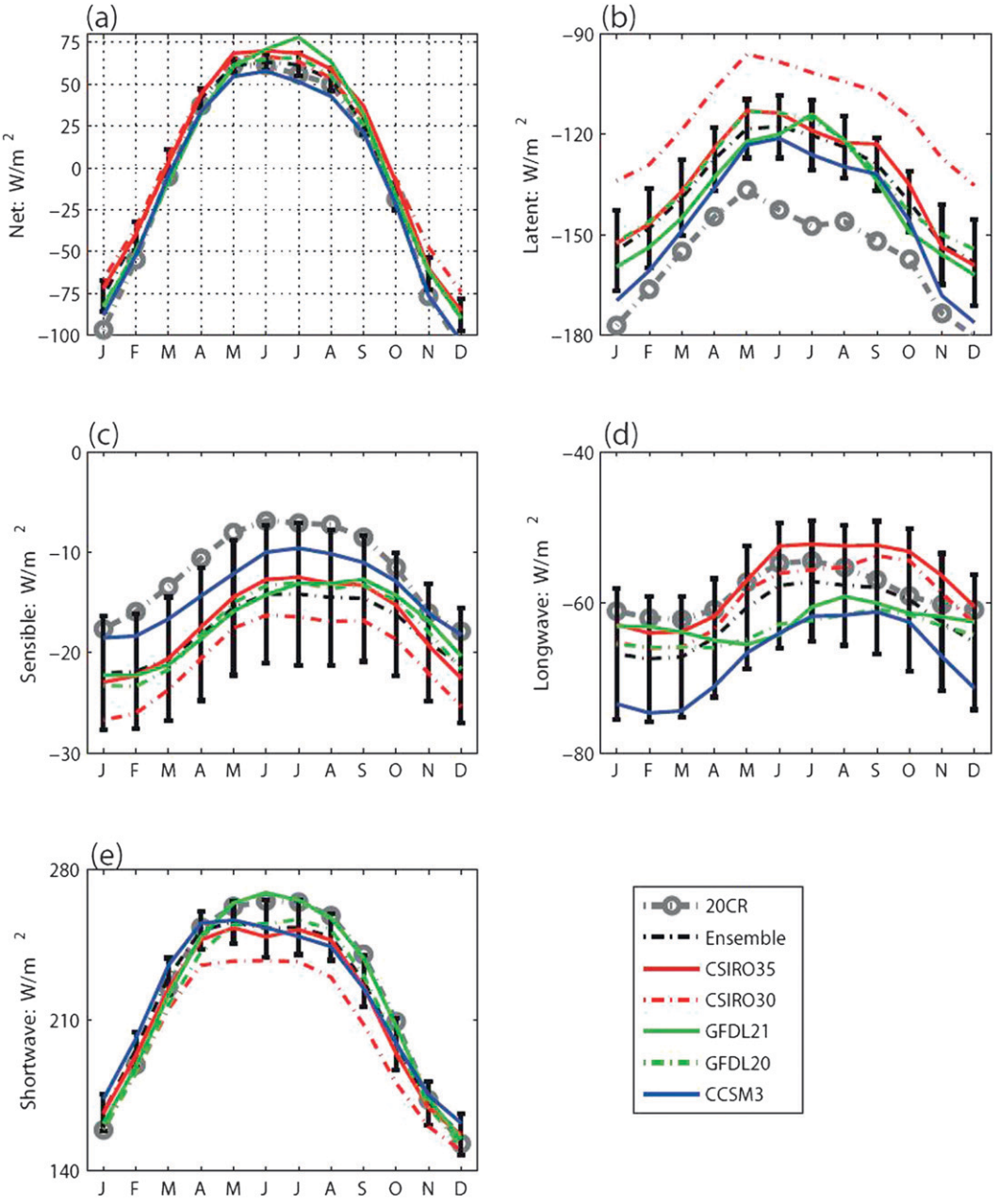

FIG. 3. Seasonal cycle of AWP box-averaged (a) net heat flux, (b) latent heat flux, (c) sensible heat flux, (d) longwave heat flux, and (e) shortwave heat flux; unit is W m^{-2}. Ensemble of 19 models is shown in black line with standard deviation bar. 20CR is shown in dash gray line. For all the heat flux components, positive values mean ocean gains heat and negative values mean ocean loses heat. Model data are from 20C3M simulations.

b. Spectrum analysis

Wavelet and power spectrum analyses of the time series of monthly AWPTI are shown in Fig. 6. Figure 6a shows the wavelet power pattern based on ERSST. There is significant energy at multidecadal periods between about 20 yr and 32 yr and longer than 32 yr, which is also shown in Fig. 6b. The spectra of most models in PIcntrl simulations, however, demonstrate peaks in interannual band (4–7 yr), decadal band (8–20 yr), and multidecadal band (20–30, 40–60 yr or longer) all with 95% significance as shown in Fig. 6c. The spectrum of the model ensemble (Fig. 6c) also reflects the four bands. Based on the global spectral character of the model ensemble, three

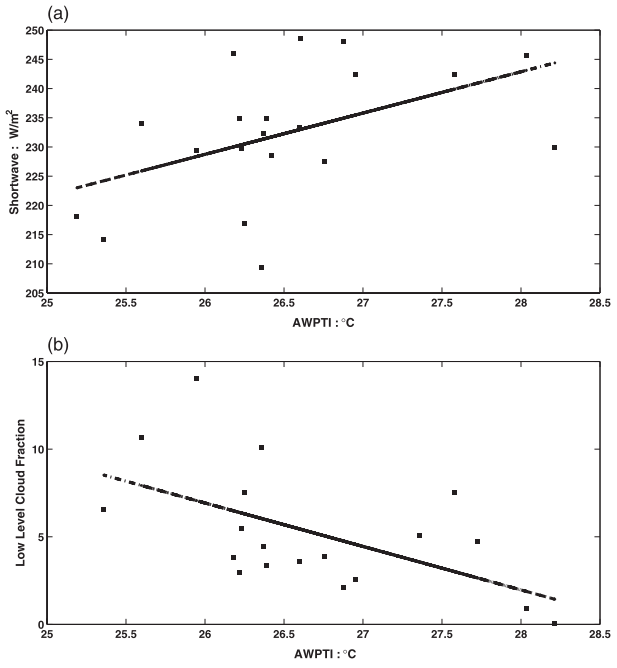

FIG. 4. Multimodel scatterplot in JASO of (a) shortwave radiation vs AWPTI and (b) low-level cloud fraction vs AWPTI. Each point stands for one model. The black line shows the least squares linear fit to all points. Model data are from 20C3M simulations.

groups of models are categorized as shown in Table 2. In Category I (as shown in Fig. 6d), four models simulate the multidecadal band and interannual band: CGCMt63, GFDL20, GFDL21, and the Institute of Atmospheric Physics (IAP). In Category II (shown in Fig. 6e), two models simulate the multidecadal band and decadal band: INMCM and CCSM3 at the 95% significance level. In Category III, 10 models—consisting of CGCMt47, CNRM, CSIRO30, GISSer, IPSL, Mhires, Mmedres, MRI, Uhadcm3, and Uhadgem1—simulate significant variability on interannual, decadal, and multidecadal, all three bands. Obviously, an important question is why the interannual band and decadal band in ERSST are not significant compared with the CGCMs. One possible explanation is that, in the AWP region, local air–sea interaction is important in determining AWP variability. Higher SST leads to increased deep convection and the convection related net heat flux tends to cool down the AWP (Wu et al. 2006). Therefore, the SST anomalies are damped and its spectrum is reddened. There is no pronounced variability, at least on interannual time scales. Then the source of low frequency variability on the multidecadal time scale is expected from oceanic processes (Delworth and Mann 2000). CGCMs, however, are limited in representing this local air–sea interaction (Wu et al. 2006; Lee et al. 2007) and show strong intrinsic variability.

In summary, spectral analysis of ERSST reveals that multidecadal variability is dominant in the AWP region. The AWP also demonstrates a moderate amplitude of interannual variability though it is not significant in ERSST. As in other characteristics, the models have varying degrees of agreement. In the next two sections, we focus on interannual and multidecadal variability of the AWP in its peak season.

c. *Interannual variability*

The AWP peaks during July–October (JASO). The ERSST time series of detrended AWPTI in JASO on interannual time scales (periods < 7 yr) (figure not shown) demonstrates a moderate amplitude of variations. But the period for this interannual variability is irregular. Each model also shows very different variability; when models are averaged, the amplitude drops due to the lack of coherence between models, thus giving a poor representation of the observed variability.

To look into the interannual variability of the AWP, we first perform an EOF analysis on the tropical Atlantic JASO SST from 30°S to 30°N, as shown in Fig. 7. The first mode of observations with 30.9% variance [Fig. 7a(1)] is a pantropical Atlantic pattern with heavier loading in the region of the Atlantic Niño mode (equatorial zonal mode), featuring maximum SST anomalies on the equator and associated changes in the easterly trade winds (Philander 1986; Zebiak 1993; Carton and Huang 1994). Between 30°S and 30°N the SST anomaly is in the same phase. The second mode is the Atlantic meridional gradient mode (AMM) with 18.1% variance [Fig. 7a(2)], which is the dominant mode in spring. The SST anomaly in the Southern Hemisphere (0°–30°S) is in opposite phase to the anomaly in the Northern Hemisphere (0°–30°N). The two corresponding principal components time series show that the periods are irregular for these modes. AWP interannual variability is primarily dominated by these two modes though the variance of these two modes in the AWP region is small. Based on nine CGCM simulations of 20C3M, Breugem et al. (2006) pointed out a common model bias: the onset of the AMM is preceded by the presence of a zonal mode in boreal fall that extends to the western boundary of the Atlantic basin and initiates a wind–evaporation–SST feedback. Hence, there is a spuriously strong interaction between the zonal and AMM mode. So it is expected that the zonal mode and AMM mode coexist in the JASO months for the CGCMs of PIcntrl and the two modes primarily dominate the AWP interannual variability in summer.

Compared with the EOF modes of ERSST, the CGCMs are categorized into four groups as shown in Table 3. Category I, consisting of CGCMt47, CGCMt63, GISSer, and Mmedres, Figs. 7b(1)–(3), successfully captures the

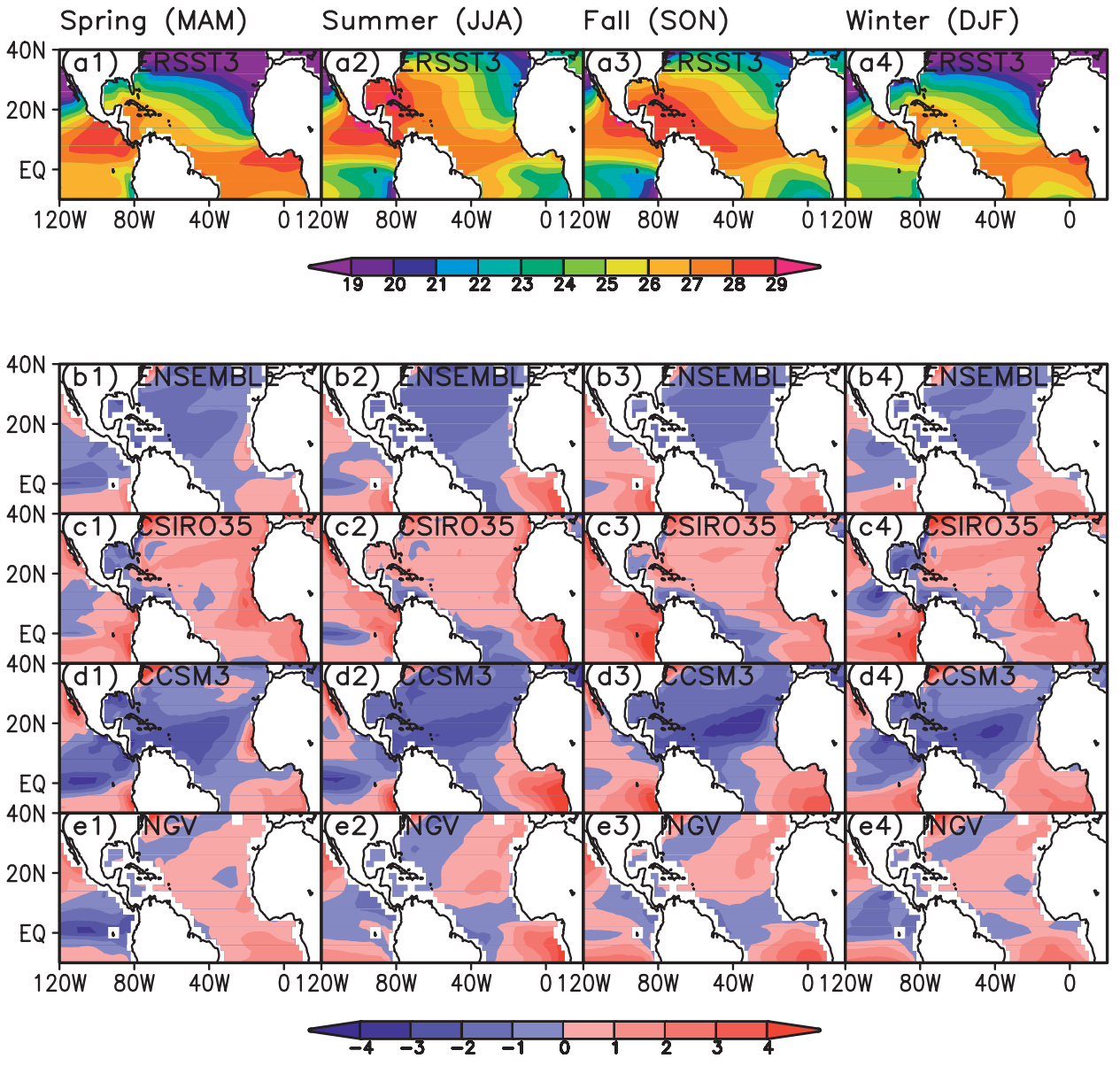

FIG. 5. Observational SST and model SST bias in four seasons. Shown are [a(1)–a(4)] ERSST SST averaged in four seasons, [b(1)–b(4)] the seasonal SST bias of the 22 model ensemble, and [c(1)–c(4), d(1)–d(4), e(1)–e(4)] the seasonal SST bias for selected models. Unit is °C. Model data are from 20C3M simulations.

zonal and meridional modes as the first two modes with the overall character of ERSST. Category II, consisting of CSIRO30, GFDL20 [Figs. 7c(1)–(3)], GFDL21, CCSM3, Uhadcm3, and Uhadgem1, is able to simulate the zonal mode as the first mode but unable to capture the meridional mode. For the zonal mode, the SST anomaly on the equator and cold tongue region is in opposite phase to the anomaly outside the equatorial region. A possible explanation for this is that the warm bias in the cold tongue and Benguela Coast region is involved in the interannual variability of CGCMs. Four models are only able to simulate correct meridional modes as the second mode: IAP, IPSL [Figs. 7d(1)–(3)], Mhires, and MRI. Category IV, including CNRM [Figs. 7e(1)–(3)] and INMCM, is not able to capture either the zonal mode as the first mode or the meridional mode as the second mode. For INMCM, the first mode should be the meridional mode and the second mode corresponds to the zonal mode.

d. Multidecadal variability

Based on the time series of detrended 7-yr moving average AWPTI in JASO (not shown), ERSST displays

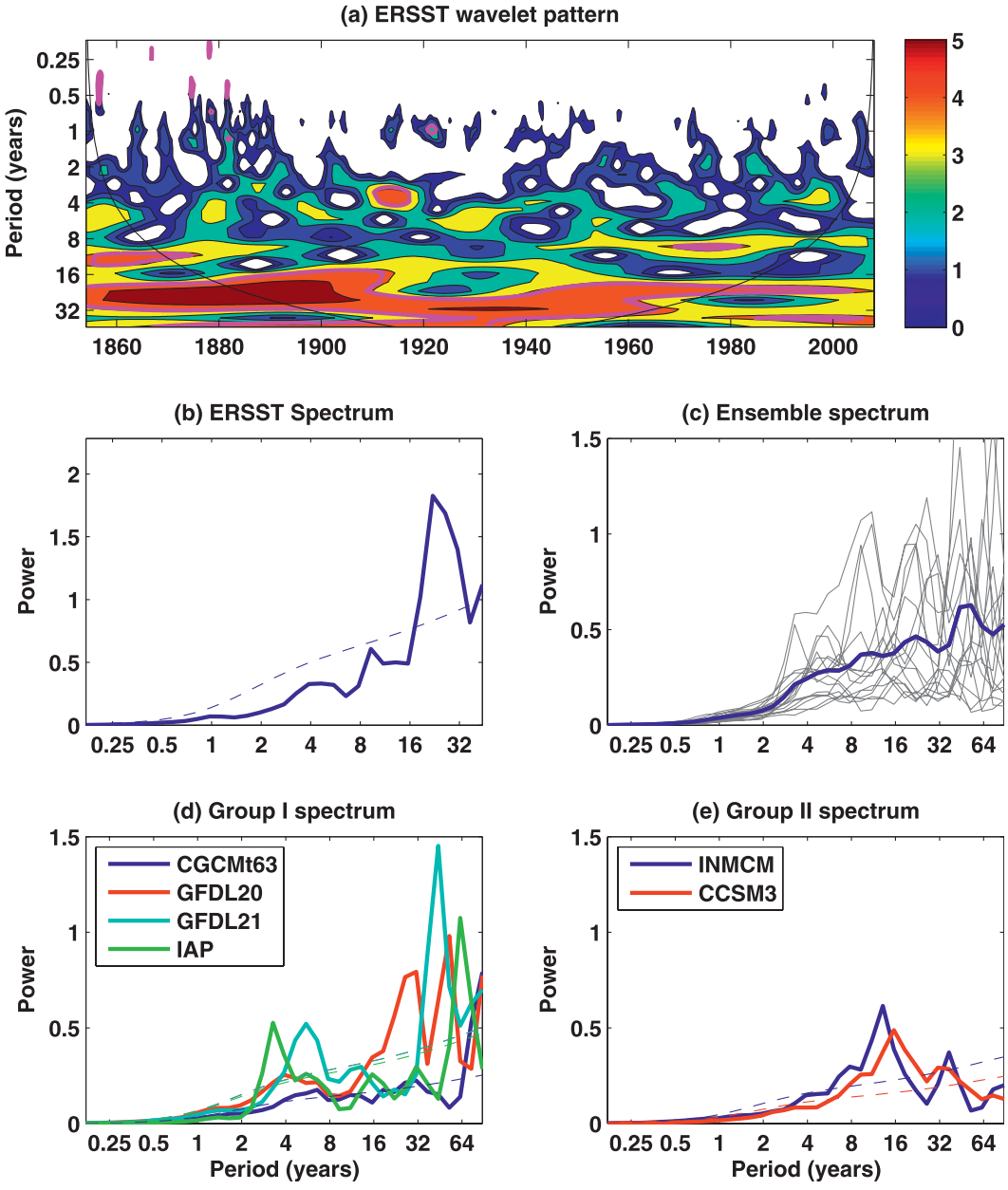

FIG. 6. Spectrum analysis of AWPTI. (a) Wavelet power spectrum of ERSST. Power above the 95% confidence level is plotted using pink contour line. *X* axis is time; *Y* axis is the wavelet period in years. (b) Global spectrum of ERSST. *Y* axis is power ($°C^2$); *X* axis is the wavelet period (yr). The dashed line indicates 95% significance level. (c),(d),(e) As in (b) but for the ensemble of 16 models with each model shown in gray line, Group I and II models respectively. Model data are from PIcntrl simulations.

a strong multidecadal variability. Three positive phases are from 1870 to 1890, 1930 to 1970, and after 1990. Models display different multidecadal variability. They are much improved compared with the performance of interannual variability but, again when models are averaged, the amplitude drops owing to the lack of coherence between models.

Based on the AWPTI of ERSST, the pattern of global SST difference between large AWP years and small AWP years on the multidecadal time scale is shown in Fig. 8a. The threshold value of AWPTI to define large (small) AWP years is 0.1°C (−0.1°C). Figure 8a suggests that a warm AWP is associated with warming almost everywhere on the global ocean but lacks the equatorial

TABLE 2. Three groups of models categorized shown in spectrum analysis.

Category	Description	Models
I	Capturing both multidecadal and decadal band with 95% significance level	CGCMt63, GFDL20, GFDL21, IAP
II	Capturing both multidecadal and decadal band with 95% significance level	INMCM, CCSM3
III	Capturing multidecadal, decadal and interannual band with 95% significance level	CGCMt47, CNRM, CSIRO30, GISSer, IPSL, Mhires, Mmedres, MRI, Uhadcm3, Uhadgem1

Pacific signature of ENSO. This pattern is identical to the pattern regressed on AWPAI of JJASO (Wang et al. 2008a), but also has global warming signature included because the linear detrending cannot remove the entire global warming signal. The spatial pattern suggests that the AWP multidecadal variability resembles the AMO, which is well supported by a close relationship between the AWP SST index (AWPTI) and Atlantic multidecadal oscillation (AMO) index. Compared with ERSST, 15 models—CGCMt47, CGCMt63, CNRM, CSIRO30, GFDL20, GFDL21, GISSer, IAP, INMCM, IPSL, Mhires, Mmedres, CCSM3, Uhadcm3 (Fig. 8c), and Uhadgem1—successfully reproduce the major characters of the observed pattern of global SST difference between large AWP years and small AWP years. For individual CGCMs and the ensemble, the threshold value of the AWPTI to define large (small) AWP years is also 0.1°C (−0.1°C). Only MRI (Fig. 8d) is not able to reproduce the observed spatial pattern. For the ensemble of 16 models, the pattern of global SST difference between large AWP years and small AWP years shown in Fig. 8b has a realistic representation of the observed AMO pattern.

e. Remote connection

Next we focus on the interannual variability of the AWP induced by remote influences. AWP variability can be remotely influenced by the ENSO and NAO. Czaja et al. (2002) and Enfield et al. (2006) studied the delayed influence of the ENSO and NAO on the tropical North Atlantic region. Here we performed a similar analysis on the AWP region to show how this remote influence acts on the AWP in CGCMs. We regress zonally averaged observed variables including surface wind stress, net surface heat flux, and SST in the AWP region on the Niño-3 SST index, Fig. 9a(1), and the negative NAO index, Fig. 9a(2), from January to December. Figure 9a(1) shows that positive ENSO events correspond to westerly low-level wind anomalies over the AWP (shown in vectors), which are largest during JFM. This wind anomaly induces heating between 5°N and 20°N over the AWP region at a rate of 8 W m^{-2} due to a decreased latent heat flux loss (shown in contour) and leads to a warm SST anomaly (shown in shading) of 0.2°C during February–May (FMAM). After May the surface wind anomaly is weakened, the anomalous surface heat flux changes sign, and the warm SST anomaly is dampened. North of 25°N the anomalous westerlies induce cooling at a rate of -8 W m^{-2} and produce a cold SST anomaly of 0.1°C during FMAM. Figure 9a(2) shows a regression pattern on the negative NAO index similar to Fig. 9a(1). But, the magnitude of the SST warming anomaly between 5° and 20°N is about 0.2°C less than the magnitude of ENSO influence. The anomalous net heat flux also changes sign after March. As suggested by Czaja et al. (2002) for the TNA analysis, a similar mechanism determines the forcing of AWP variability in spring by both the ENSO and NAO. Thus, to some extent, the AWP region can be regarded as an extension of the tropical North Atlantic under the influence of ENSO and the NAO.

Compared with the above observational analysis, only five models, identified as Category I in Table 4, are able to successfully capture the major features for the remote influence from both ENSO and NAO influences: CGCMt47, IAP [Figs. 9c(1),(2)], IPSL, Mhires and MRI. Seven models in Category II are able to capture the major character of the NAO influence: CGCMt63, CNRM, GFDL20 GFDL21 [Figs. 9d(1),(2)], GISSer, Mmedres, Uhadcm3, and Uhadgem1. In these models, the wind–evaporation–SST mechanism still holds true in explaining the processes. However, the process of warming and cooling phase between 5° and 20°N for the ENSO influence is not captured. Only one model, INMCM in Category III, cannot simulate the observed regression patterns for either the ENSO or NAO. For the ENSO regression in INMCM, the wind–evaporation–SST mechanism can explain the warming induced by ENSO, but the warming center is located at the equator. Thus, because of the limitations of the models, most CGCMs are unable to reliably simulate the remote patterns of influence in the AWP region induced by ENSO and the NAO. Nevertheless, the ensemble of the 14 analyzed models successfully simulates the observed remote influence pattern in the AWP region induced by both ENSO, Fig. 9b(1), and the NAO, Fig. 9b(2).

In Fig. 10, a Taylor diagram is constructed using the regression coefficients of SST onto the Niño-3

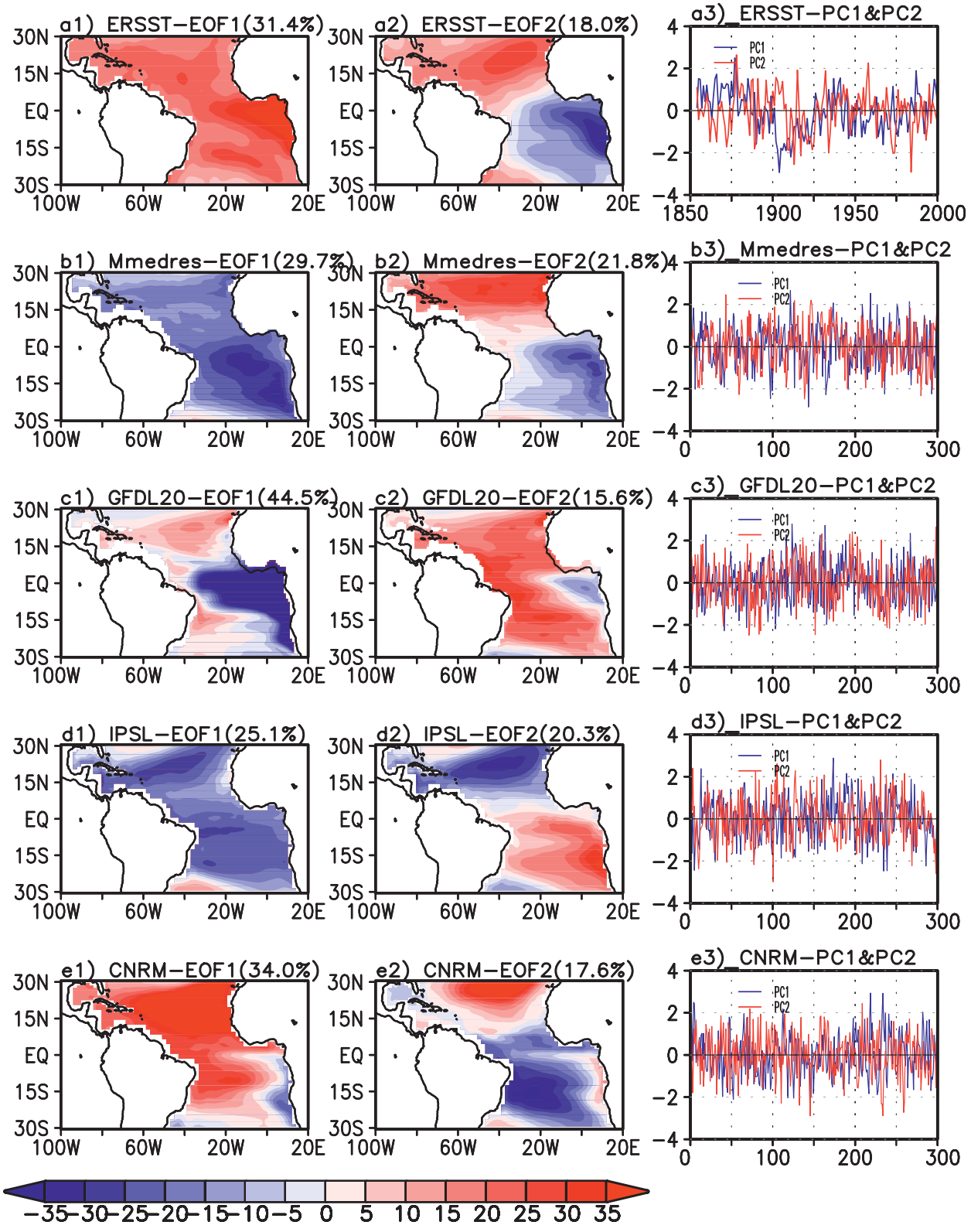

FIG. 7. EOF analysis of tropical Atlantic SST in JASO months. Unit of spatial function is 10^{-2}. Shown are [a(1)] first mode of ERSST, [a(2)] second mode of ERSST, and [a(3)] PC1 and PC2 of ERSST. [b(1)–(3)] for Mmedres, [c(1)–(3)] for GFDL20, [d(1)–(3)] for IPSL and [e(1)–(3)] for CNRM represent four categories of CGCMs defined in Table 4, respectively. Model data are from PIcntrl simulations.

TABLE 3. Four groups of models categorized based on performance shown in EOF analysis compared with observations.

Category	Description	Models
I	Best performance with capturing zonal mode and meridional mode with the major characters of ERSST	CGCMt47, CGCMt63, GISSer, Mmedres
II	Capturing zonal mode but spatial pattern of zonal mode is not in the same phase. Unable to capture the meridional mode as the second mode.	CSIRO30, GFDL20, GFDL21, CCSM3, Uhadcm3, Uhadgem1
III	Able to capture the meridional mode as the second mode and no zonal mode is captured as the first mode	IAP, IPSL, Mhires, MRI
IV	Unable to capture both zonal mode as the first mode and meridional mode as the second mode (INMCM: first mode is meridional mode and second mode is zonal mode)	CNRM, INMCM

[December–February (DJF)] at all grid points within the AWP box: that is, the correlation between each model and observations is calculated between the regression coefficients at each grid point of model and the regressions coefficients at same grid points of observation. The standard deviation for the statistics of each model is divided by the standard deviation of observations. The reference point ''A'' for perfect correspondence of models to observations is at the (1, 1) point of standard deviation and correlation coefficient coordinates.

If the point of a model in the diagram is closer to the reference point, then the model has a better performance in representing the observed SST field. By this metric GFDL21 (I) and IPSL (O) are the models that best replicate the AWP connection to ENSO. Except for IPSL (O), the other best four models in Table 4—CGCMt47 (C), IAP (L), Mhires (P), and MRI (S)—did not show good performance in the Taylor diagram. The difference can be mainly explained as Table 4 is summarized based on zonal-averaged SST regression on the Niño-3 index.

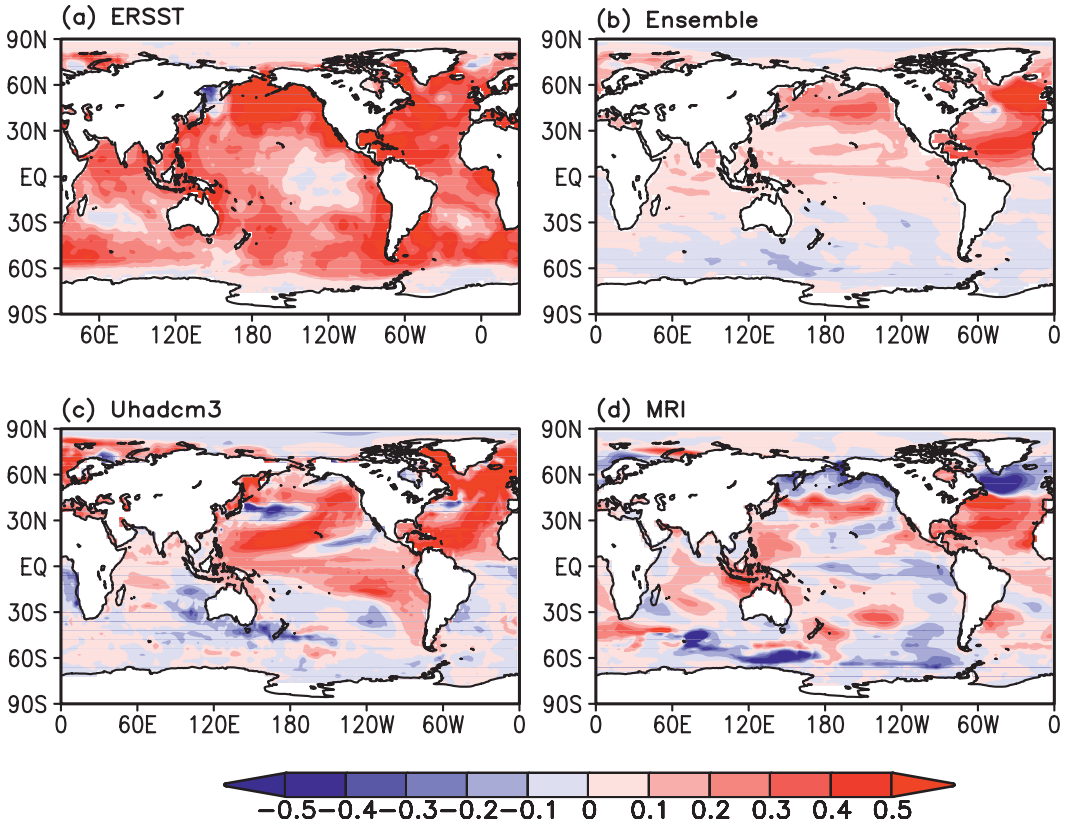

FIG. 8. Pattern of global SST difference between large AWP years and small AWP years on the decadal time scale and above. Shown are (a) ERSST, (b) ensemble of 16 models, (c) Uhadcm3 and (d) MRI. Unit is °C. For ERSST and CGCMs, the threshold value of AWPTI to define large (small) AWP years is 0.1°C (−0.1°C). Model data are from PIcntrl simulations.

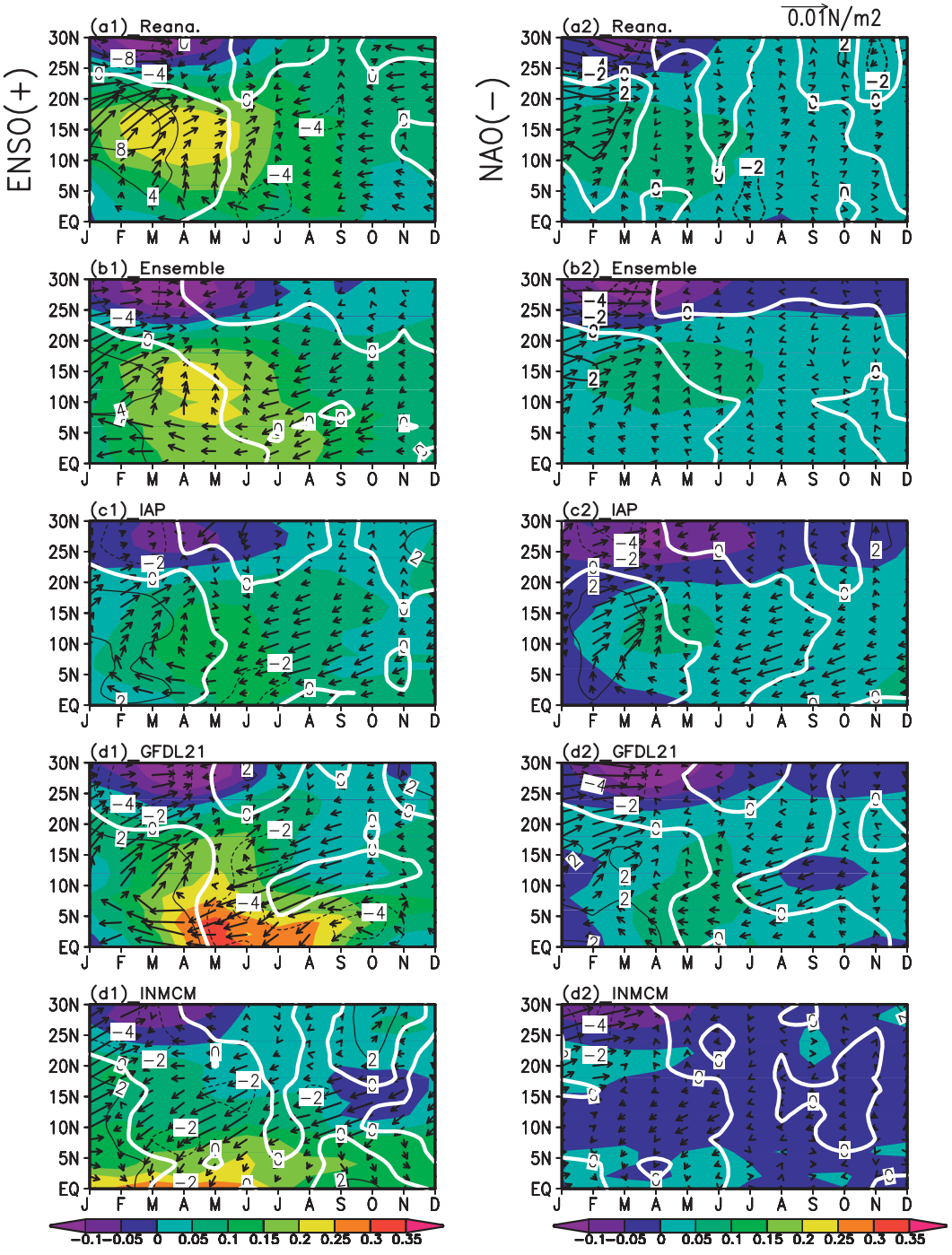

FIG. 9. Regression map of surface wind stress (vector), net surface heat flux (positive into the ocean with solid contour line), and SST (shading contour) averaged in longitude onto Niño-3 index (DJF) and onto negative NAO index (DJFM). Shown are [a(1)] regression map onto Niño-3 index for observations, [a(2)] regression map onto negative NAO Index for observations, [b(1)] regression map onto Niño-3 index for ensemble of 22 models, [b(2)] regression map onto negative NAO Index for ensemble, and (c),(d),(e) are as in (b) but for IAP, GFDL21, and INMCM, respectively. Model data are from PIcntrl simulations.

TABLE 4. Three groups of models categorized based on performance shown in AWP remote connection analysis with ENSO and NAO. (Note only 14 models are included because of data availability).

Category	Description	Models
I	Best performance with capturing the major characters for both ENSO and NAO influences	CGCMt47, IAP, IPSL, Mhires, MRI
II	Only able to capture the major character of NAO influence	CGCMt63, CNRM, GFDL20, GFDL21, GISSer, Mmedres, Uhadcm3, Uhadgem1
III	Unable to capture correct regression patterns for both ENSO and NAO	INMCM

The regression does not have a zonal pattern and shows the time lag characters between the AWP and Niño-3 index; Fig. 10 of the Taylor diagram demonstrates the SST regression of each grid point in the two dimensional AWP box on Niño-3 index. The regression reveals the spatial characters of the AWP of MAM influenced by ENSO. An interesting point to note is that models such as MRI (S) successfully capture the physical process as to how ENSO influences the AWP SST in spring, but the mean value and phase of regression coefficients across grid points with the AWP index is quite different from observations. Then, in the Taylor diagram, it is regarded as a poorly performing model. Thus, from the perspective of physical processes, conclusions drawn from Table 4 still hold true in our analysis.

Figure 11 is the same as Fig. 10 except that the statistics are defined as regression coefficients of SST onto the NAO (DJFM) index at all grid points within the AWP box. Mmedres (Q) and GISSer (K) are the best two models compared with the reference point for observations. The models, CGCMt47 (C), IAP (L), IPSL (O), Mhires (P), and MRI (S) of Category I in Table 4, also show good performances in this Taylor diagram. Comparison between Fig. 10 and Fig. 11 indicates that the selected 16 IPCC models demonstrate a better performance in simulating a remote influence pattern in the AWP region induced by the NAO than the performance in simulating the influence induced by ENSO. This conclusion is also reflected in the regression patterns of the model ensemble mean in Fig. 9b(1) and Fig. 9b(2).

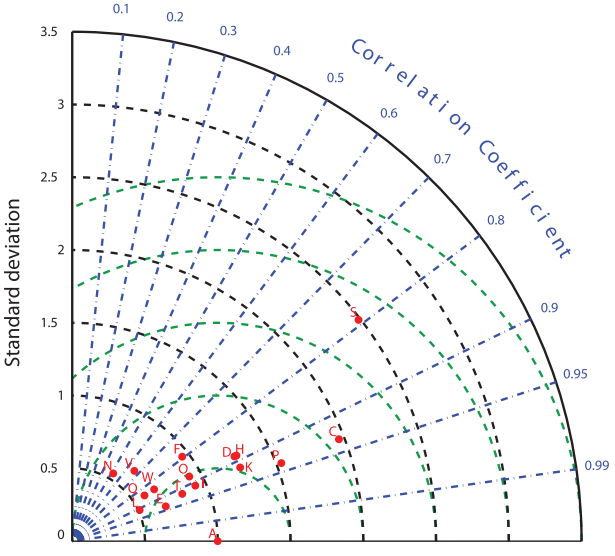

FIG. 10. A Taylor diagram of statistics describing the SST (MAM) regression coefficient at each grid point within AWP box on Niño-3 (DJF) index for the observation and 16 IPCC models. On this diagram, the radial coordinate gives the magnitude of total standard deviation of regression coefficients within AWP box for each model normalized by the standard deviation of observation, and the angular coordinate gives the correlation of the regression coefficients of each model with the regression coefficients of observation. The distance between the reference point ''A'' of observation and any model's point (B to W defined in Table 1) is proportional to the rms error shown by the green dashed lines. Model data are from PIcntrl simulations.

4. Summary and discussion

In this paper we explore AWP variability in 22 CGCMs from the IPCC AR4 database and validate them against

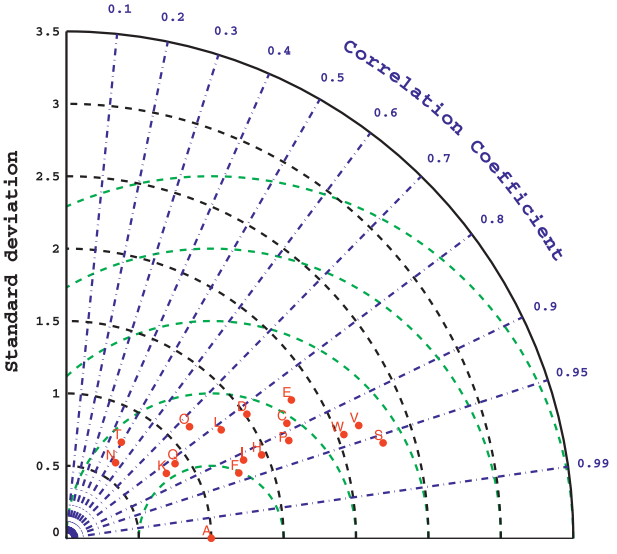

FIG. 11. As in Fig. 10 but for pattern statistics describing the SST (MAM) regression coefficient at each grid point within theAWP box on the NAO (DJFM) index for the observation and 16 IPCC models. Model data are from PIcntrl simulations.

TABLE 5. Summary of best performance models in each aspect of variability evaluation.

Criteria	Best performance models
Seasonal cycle	CSIRO35, MPI, Uhadcm3
EOF analysis	CGCMt47, CGCMt63, GISSer Mmedres
Remote connection with ENSO and NAO	CGCMt47, IAP, IPSL, Mhires, MRI
Multidecadal variability	CGCMt47, CGCMt63, CNRM, CSIRO30, GFDL20, GFDL21, GISSer, IAP, INMCM, IPSL, Mhires, Mmedres, CCSM3, Uhadcm3, and Uhadgem1

observations over the twentieth century at seasonal, interannual, and multidecadal time scales, as well as for the remote connections with the ENSO and NAO. Both the AWP area index and AWP SST index are defined to study the seasonal cycle. Three models, CSIRO35, MPI, and Uhadcm3, have the best performance in simulating the AWP seasonal cycle based on both indexes. The AWPAI is almost zero for some models in most years due to the cold SST bias found in the northern tropics for most models. Thus, we have chosen a SST index as a more effective but equivalent proxy for AWP variability. Analysis of the AWP remote connection with the ENSO and NAO shows that CGCMt47, IAP, IPSL, Mhires, and MRI are the best group of models in simulating the processes by which ENSO and NAO influence the AWP region through wind–evaporation–SST interactions. Fifteen models included in multidecadal variability evaluation, Table 5, successfully capture the spatial characters of global SST between large AWP years and small AWP years. All of the best models in each evaluation aspect are summarized in Table 5. No single model is able to simulate AWP variability of observations in all respects. An encouraging point is that at least there is always one group of CGCMs in IPCC AR4 that are able to represent well at least one aspect of AWP variability. Based on Table 5, CGCMt47 particularly shows very good performance in AWP variability, overall. As physics and configurations for every CGCM are different, the results presented in this study provide a useful reference in improving CGCM simulation of the AWP.

As discussed with respect to the AWP seasonal cycle, the cold SST bias in the AWP region appears in 19 of the 22 CGCMs. The warm SST bias in the cold tongue and Benguela Coast region exists in all 22 models. A recent paper (Richter et al. 2011) based on the GFDL CM2.1 simulation suggests that a significant portion of the equatorial SST biases in the model is due to weaker than observed equatorial easterlies during boreal spring, which reduces the tilt of the equatorial thermocline with deepening in the east and prevents cold tongue formation there in the following season. In Fig. 5, however, the warm SST bias in the cold tongue region is consistent, to some extent, in all four seasons. For the majority of 19 models, the southeast tropical Atlantic warm SST bias coincides with a cold SST bias in the AWP region, suggesting that the two regions may be linked through the Atlantic meridional gradient mode (WES feedback). Hence, the causes of Atlantic SST bias require further study. As the performance in simulating AWP variability through CGCMs is still poor, it is expected that the ability to simulate AWP impacts on the climate, such as precipitation and moisture transportation processes, is quite limited.

Acknowledgments. We thank two anonymous reviewers for their thoughtful comments and suggestions. This work was supported by grants from the National Oceanic and Atmospheric Administration's Climate Program Office and by grants from the National Science Foundation.

REFERENCES

Bell, G. D., and M. Chelliah, 2006: Leading tropical modes associated with interannual and multidecadal fluctuations in North Atlantic hurricane activity. *J. Climate,* **19,** 590–612.

Breugem, W.-P., W. Hazeleger, and R. J. Haarsma, 2006: Multimodel study of tropical Atlantic variability and change. *Geophys. Res. Lett.,* **33,** L23706, doi:10.1029/2006GL027831.

——, P. Chang, C. J. Jang, J. Mignot, and W. Hazeleger, 2008: Barrier layers and tropical Atlantic SST biases in coupled GCMs. *Tellus,* **60A,** 885–897, doi:10.1111/j.1600-0870.2008.00343.x.

Carton, J. A., and B. H. Huang, 1994: Warm events in the tropical Atlantic. *J. Phys. Oceanogr.,* **24,** 888–903.

Chang, C.-Y., J. A. Carton, S. A. Grodsky, and S. Nigam, 2007: Seasonal climate of the tropical Atlantic sector in the NCAR Community Climate System Model 3: Error structure and probable causes of errors. *J. Climate,* **20,** 1053–1070.

Chang, P., L. Ji, and H. Li, 1997: A decadal climate variation in the tropical Atlantic Ocean from thermodynamic air-sea interactions. *Nature,* **385,** 516–518.

Compo, G. P., and Coauthors, 2011: The Twentieth Century Reanalysis Project. *Quart. J. Roy. Meteor. Soc.,* **137,** 1–28, doi:10.1002/qj.776.

Covey, D., and S. Hastenrath, 1978: The Pacific El Niño phenomenon and the Atlantic circulation. *Mon. Wea. Rev.,* **106,** 1280–1287.

Czaja, A., P. van der Vaart, and J. Marshall, 2002: A diagnostic study of the role of remote forcing in tropical Atlantic variability. *J. Climate,* **15,** 3280–3290.

Delworth, T. L., and M. E. Mann, 2000: Observed and simulated multidecadal variability in the Northern Hemisphere. *Climate Dyn.,* **16,** 661–676.

——, and Coauthors, 2006: GFDL's CM2 global coupled climate models. Part I: Formulation and simulation characteristics. *J. Climate,* **19,** 643–674.

de Szoeke, S. P., and S.-P. Xie, 2008: The tropical eastern Pacific seasonal cycle: Assessment of errors and mechanisms in IPCC

AR4 coupled ocean–atmosphere general circulation models. *J. Climate,* **21,** 2573–2590.

Enfield, D. B., and D. A. Mayer, 1997: Tropical Atlantic sea surface temperature variability and its relation to El Niño–Southern Oscillation. *J. Geophys. Res.,* **102** (C1), 929–945.

——, and S.-K. Lee, 2005: The heat balance of the Western Hemisphere warm pool. *J. Climate,* **18,** 2662–2681.

——, A. M. Mestas-Nuñez, D. A. Mayer, and L. Cid-Serrano, 1999: How ubiquitous is the dipole relationship in tropical Atlantic sea surface temperatures? *J. Geophys. Res.,* **104** (C4), 7841–7848.

——, ——, and P. J. Trimble, 2001: The Atlantic multidecadal oscillation and its relation to rainfall and river flows in the continental U.S. *Geophys. Res. Lett.,* **28,** 2077–2080.

——, S.-K. Lee, and C. Wang, 2006: How are large Western Hemisphere warm pools formed? *Prog. Oceanogr.,* **70** (2–4), 346–365.

Giannini, A., M. A. Cane, and Y. Kushnir, 2001: Interdecadal changes in the ENSO teleconnection to the Caribbean region and the North Atlantic Oscillation. *J. Climate,* **14,** 2867–2879.

Goldenberg, S. B., C. W. Landsea, A. M. Mesta-Nuñez, and W. M. Gray, 2001: The recent increase in Atlantic hurricane activity: Causes and implications. *Science,* **293,** 474–479.

Gordon, H., S. O'Farrell, M. Collier, M. Dix, L. Rotstayn, E. Kowalczyk, T. Hirst, and I. Watterson, 2010: The CSIRO Mk3.5 climate model. CAWCR Tech. Rep. 021, 74 pp.

Grotzner, A., M. Latif, and T. P. Barnett, 1998: A decadal climate cycle in the North Atlantic Ocean as simulated by the ECHO coupled GCM. *J. Climate,* **11,** 831–847.

Guilyardi, E., A. Wittenberg, A. Fedorov, M. Collins, C. Wang, A. Capotondi, G. J. van Oldenborgh, and T. Stockdale, 2009: Understanding El Niño in ocean–atmosphere general circulation models: Progress and challenges. *Bull. Amer. Meteor. Soc.,* **90,** 325–340.

Hurrell, J. W., 1995: Decadal trends in the North Atlantic Oscillation: Regional temperatures and precipitation. *Science,* **269,** 676–679.

Joseph, R., and S. Nigam, 2006: ENSO evolution and teleconnections in IPCC's 20th century climate simulations: Realistic representation? *J. Climate,* **19,** 4360–4377.

Latif, M., and A. Grötzner, 2000: On the equatorial Atlantic oscillation and its response to ENSO. *Climate Dyn.,* **16,** 213–218.

Lee, S.-K., D. B. Enfield, and C. Wang, 2007: What drives seasonal onset and decay of the Western Hemisphere warm pool? *J. Climate,* **20,** 2133–2146.

——, ——, ——, 2008: Why do some El Niños have no impact on tropical North Atlantic SST? *Geophys Res. Lett.,* **35,** L16705, doi:10.1029/2008GL034734.

——, C. Wang, and B. E. Mapes, 2009: A simple atmospheric model of the local and teleconnection responses to tropical heating anomalies. *J. Climate,* **22,** 272–284.

Lin, J.-L., 2007: The double-ITCZ problem in IPCC AR4 coupled GCMs: Ocean–atmosphere feedback analysis. *J. Climate,* **20,** 4497–4525.

——, and Coauthors, 2006: Tropical intraseasonal variability in 14 IPCC AR4 climate models. Part I: Convective signals. *J. Climate,* **19,** 2665–2690.

Mansbach, D. K., and J. R. Norris, 2007: Low-level cloud variability over the equatorial cold tongue in observations and models. *J. Climate,* **20,** 1555–1570.

Miller, R. L., and Coauthors, 2006: Mineral dust aerosols in the NASA Goddard Institute for Space Sciences Model E atmospheric general circulation model. *J. Geophys. Res.,* **111,** D06208, doi:10.1029/2005JD005796.

Misra, V., S. Chan, R. Wu, and E. Chassignet, 2009: Air–sea interaction over the Atlantic warm pool in the NCEP CFS. *Geophys. Res. Lett.,* **36,** L15702, doi:10.1029/2009GL038737.

Nobre, P., and J. Shukla, 1996: Variations in sea surface temperature, wind stress, and rainfall over the tropical Atlantic and South America. *J. Climate,* **9,** 2464–2479.

Okumura, Y., and S.-P. Xie, 2006: Some overlooked features of tropical Atlantic climate leading to a new Niño-like phenomenon. *J. Climate,* **19,** 5859–5874.

Philander, S. G. H., 1986: Predictability of El Niño. *Nature,* **321,** 810–811.

Richter, I., and S.-P. Xie, 2008: On the origin of equatorial Atlantic biases in coupled general circulation models. *Climate Dyn.,* **31,** 587–598.

——, and Coauthors, 2011: Tropical Atlantic biases and their relation to surface wind stress and terrestrial precipitation. *Climate Dyn.,* **38,** 985–1001.

Saji, N. H., S.-P. Xie, and T. Yamagata, 2006: Tropical Indian Ocean variability in the IPCC twentieth-century climate simulations. *J. Climate,* **19,** 4397–4417.

Servain, J., 1991: Simple climate indices for the tropical Atlantic Ocean and some applications. *J. Geophys. Res.,* **96** (C8), 15 137–15 146.

Smith, T .M., R. W. Reynolds, T. C. Peterson, and J. Lawrimore, 2008: Improvements to NOAA's historical merged land–ocean surface temperature analysis (1880–2006). *J. Climate,* **21,** 2283–2296.

Taylor, K. E., 2001: Summarizing multiple aspects of model performance in a single diagram. *J. Geophys. Res.,* **106** (D7), 7183–7192.

Torrence, C., and G. P. Compo, 1998: A practical guide to wavelet analysis. *Bull. Amer. Meteor. Soc.,* **79,** 61–78.

Wang, C., and D. B. Enfield, 2001: The tropical Western Hemisphere warm pool. *Geophys. Res. Lett.,* **28,** 1635–1638.

——, and ——, 2003: A further study of the tropical Western Hemisphere warm pool. *J. Climate,* **16,** 1476–1493.

——, ——, S.-K. Lee, and C. W. Landsea, 2006: Influences of the Atlantic warm pool on Western Hemisphere summer rainfall and Atlantic hurricanes. *J. Climate,* **19,** 3011–3028.

——, S.-K. Lee, and D. B. Enfield, 2008a: Atlantic warm pool acting as a link between Atlantic multidecadal oscillation and Atlantic tropical cyclone activity. *Geochem. Geophys. Geosyst.,* **9,** Q05V03, doi:10.1029/2007GC001809.

——, ——, and ——, 2008b: Climate response to anomalously large and small Atlantic warm pools during the summer. *J. Climate,* **21,** 2437–2450.

——, H. Liu, S.-K. Lee, and R. Atlas, 2011: Impact of the Atlantic warm pool on United States landfalling hurricanes. *Geophys. Res. Lett.,* **38,** L19702, doi:10.1029/2011GL049265.

Wu, R., B. P. Kirtman, and K. Pegion, 2006: Local air–sea relationship in observations and model simulations. *J. Climate,* **19,** 4914–4932.

Xie, S.-P., and J. A. Carton, 2004: Tropical Atlantic variability: Patterns, mechanisms, and impacts. *Ocean–Atmosphere Interaction and Climate Variability, Geophys. Monogr.,* Vol. 147, Amer. Geophys. Union, 121–142.

——, Y. Tanimoto, H. Noguchi, and T. Matsuno, 1999: How and why climate variability differs between the tropical Atlantic and Pacific. *Geophys. Res. Lett.,* **26,** 1609–1612.

Zebiak, S. E., 1993: Air–sea interaction in the equatorial Atlantic region. *J. Climate,* **6,** 1567–1586.